Journal of Hazardous Materials 192 (2011) 1667–1674

Contents lists available at ScienceDirect

Journal of Hazardous Materials

journal homepage: www.elsevier.com/locate/jhazmat

In situ incorporation of nickel nanoparticles into the mesopores of MCM-41 by manipulation of solvent–solute interaction and its activity toward adsorptive desulfurization of gas oil

Abdolraouf Samadi-Maybodi[a,*], Mohammad Teymouri[b], Amir Vahid[a], Aliakbar Miranbeigi[c]

[a] Analytical Division, Faculty of Chemistry, University of Mazandaran, Babolsar, Iran
[b] Research Institute of Petroleum Industry, Tehran, Iran
[c] Petroleum Refining Division, Research Institute of Petroleum Industry, Tehran, Iran

ARTICLE INFO

Article history:
Received 20 March 2011
Received in revised form 29 June 2011
Accepted 30 June 2011
Available online 6 July 2011

Keywords:
Mesoporous silica
Nickel nanoparticles
Adsorptive desulfurization
In situ incorporation

ABSTRACT

In this contribution, different amounts of nickel were incorporated into the mesopores of MCM-41 via an in situ approach. A hydrophobic nickel precursor was incorporated into the nanochannels of mesoporous silica by manipulation of solvent–solute interaction. The synthesized material was characterized using X-ray diffraction, nitrogen physisorption, temperature programmed reduction, and transmission electron microscopy. The results implicate the formation of MCM-41 with well-ordered hexagonal structure and establish also the presence of nickel nanoparticles inside the nanochannels of mesoporous silica. Adsorptive desulfurization of gas oil was conducted using the nickel-incorporated MCM-41 samples. The effects of nickel concentration, temperature of process and feed flow rate on the desulfurization process were examined. The MCM-41 containing 6 wt.% of nickel had both the highest breakthrough sulfur adsorption capacity and total sulfur adsorption capacity, which were 0.69 and 1.67 mg sulfur/g adsorbent, respectively. The breakthrough sulfur adsorption capacity was almost regained after reductive regeneration of spent adsorbent. The obtained results suggest that the method applied for the synthesis of Niy/MCM resulted in formation of well-dispersed, accessible and small nickel nanoparticles incorporated into the pores of MCM-41 which might be an advantage for adsorption of refractory sulfur compounds from low sulfur gas oil.

1. Introduction

MCM-41 is a mesoporous molecular sieve which formed from the closely packed silica-coated micelles of a surfactant template [1,2]. Because of its unique structural and physical properties; notably large surface area, tunable and large pore size, narrow pore size distribution and high thermal stability [3–5], MCM-41 has attracted great attention in many fields such as catalysis [6], separation [7], optics [8], medicine [9], and desulfurization [10,11]. But one of the main drawbacks of this material is its low activity in many reactions such as acid catalyst [4,6]. This low activity can be overcome by functionalization of MCM-41 by organic and inorganic species such as metal nanoparticles, organometalic complexes and enzymes [6]. There are many synthetic strategies for the in situ or post-synthesis functionalization of mesoporous materials by metallic nanoparticles. In the former case, the most usual method is doping of reaction mélange with metal salts [12–15]. In post-synthetic approach, the most common synthesis routes are I: incipient wetness impregnation [16], II: ion exchange [17], III: equilibrium adsorption [18], IV: metal complex immobilization [19], V: vapor phase deposition [20] and VI: sonication [21–24].

One of the main applications of metal-containing mesoporous silica is the desulfurization of transport fuels [25–27]. As a result of increasingly stringent environmental regulations concerning the sulfur content in transportation fuels and the heightened interest for cleaner air, refiners are facing the inevitable reality that they will soon need to produce clean automotive fuels with ultralow sulfur levels. The current hydrotreating technology has it difficult to reduce the sulfur content in diesel to less than 10 ppmw, because the remaining refractory sulfur compounds such as dibenzothiophene are not easy to remove [28,29]. Alternative methods such as adsorptive desulfurization, oxidative and extractive desulfurization, biodesulfurization, etc. are being developed in recent years to produce ultra low sulfur fuels. Adsorptive desulfurization of gas oil is a promising alternative to the conventional hydrodesulfurization process used on a large scale in petroleum refining industry but in most cases it cannot attain the ultra low sulfur content of below 10 ppmw [30]. Some efforts have been conducted for adsorptive

* Corresponding author. Tel.: +98 1125342350; fax: +98 1125342350.
E-mail address: samadi@umz.ac.ir (A. Samadi-Maybodi).

0304-3894/$ – see front matter © 2011 Elsevier B.V. All rights reserved.
doi:10.1016/j.jhazmat.2011.06.089

desulfurization of gas oil using mesoporous silica and zeolite which were doped with nickel via a simple method, i.e., impregnation [31–33].

In this work, we report incorporation of nickel into the mesopores of MCM-41 material via a modified in situ method by manipulation of solvent–solute interaction. This method results in formation of nickel nanoparticles inside the mesopores of MCM-41 rather than random distribution of them throughout the wall structure of MCM-41 while structural order of the MCM-41 remains almost intact. Incorporation of nickel precursor (nickel acetylacetonate) into the mesopores of MCM-41 leads to the controlled growth of nanoparticles. After that, in order to investigate the capacity of the synthesized samples for reducing the sulfur level in a commercial gas oil for environmental protection, deep desulfurization is conducted in a flow system using synthesized nickel-containing MCM-41 samples as adsorbent. The regeneration of the spent adsorbent is also examined via reduction route by hydrogen gas.

2. Experimental

2.1. Materials and methods

All chemical compounds were purchased from Merck and used as purchased without any purification.

The nickel acetylacetonate ($Ni(acac)_2$) was dissolved in toluene and used as nickel precursor. In a typical synthesis, cetyltrimethylammonium bromide (CTAB) was dissolved in an appropriate amount of deionized water and ethanol. While steering (at 500 rpm), the nickel precursor was added to the surfactant solution. Then, ammonia solution and sodium acetate was added followed by stirring for 30 min. About 90 vol.% of ethanol of solution was distilled under vacuum at 50 °C. TEOS was added to the above solution and steered for 2.5 h. The obtained suspension was transferred into the Teflon-lined stainless steel and autoclaved at 70 °C for 8 h. The final molar composition of the mixture was $(1 + 5x)$ TEOS, 0.3 CTAB, 1.5 sodium acetate, 1 ethanol, 14 NH_3, 20 H_2O, x Ni while x representing the molar ratio of Ni/Si in the corresponding sample. Then the precipitate was filtered and washed with deionized water and dried in oven at 70 °C over night. The synthesized samples calcined at 500 °C under air for 5 h with a heating rate of 1 °C/min from room temperature to 500 °C. The samples denoted as Niy/MCM where y represents the percentage of nickel weight with respect to that of MCM-41 in the corresponding sample. The quantity of y was determined by classical wet chemistry methods with an atomic absorption spectrometer.

2.2. Desulfurization process

The feed stock was a commercial ultra low sulfur diesel (from Tehran refinery, Iran with sulfur concentration less than 1 ppmw) which was doped with 300 ppmw of 4-methyldibenzothiophene (MDBT). The effects of three effective factors, i.e., the concentration of nickel (3, 6 and 7 wt.%), temperature and flow rate were investigated. The adsorption experiments were carried out at four temperatures (25, 75, 150, 200 °C) and two flow rates (0.3 and 1 ml/min) on the three synthesized adsorbents. A single-channel flowing adsorption device was used for both screening adsorbents and regenerating the spent adsorbents. A stainless steel column with an internal diameter of 4.6 mm and length of 250 mm was used. A tubular furnace was equipped for heat treatment, temperature maintenance and regeneration of spent adsorbent. A measured quantity of adsorbent was packed in the column. Before feeding the gas oil, the Niy/MCM (adsorbent) were heated up to 350 °C in N_2 flow and then reduced in situ for 2 h using 50% H_2 in N_2 at a rate of 20 ml/min. After the pretreatment, the temperature of the adsorbent bed was reduced to 25 °C for the subsequent adsorption experiments. Gas oil was sent into the adsorbent column by a HPLC pump, at two flow rates (0.3 and 1 ml/min). The effluent from the top of the column was collected periodically analyzed via an ELEMENTAR Vario trace total sulfur analyzer. For the breakthrough test, 10 ppmw was taken as the criterion for the sulfur breakthrough. Breakthrough sulfur adsorption capacity was defined as the integrated area between the breakthrough curve and the straight line, representing the 10 ppm sulfur concentration of the feed. Similarly, total sulfur adsorption capacity was defined as the integrated area between the breakthrough curve and the straight line, representing the initial (300) ppm sulfur concentration of the feed.

2.3. Characterization

X-ray diffraction (XRD) patterns were recorded by a GBC MMA diffractometer with beryllium-filtered Cu Kα radiation (1.5418 Å) operating at 35.4 kV and 28 mA. Diffraction data were recorded between 1 and 10° 2θ with a resolution of 0.01° 2θ with the scan rate of 0.5 2θ/min. The chemical analysis for the determination of nickel concentration in synthesized samples was performed with a PerkinElmer AAnalyst 400 spectrometer. Physisorption of nitrogen was measured at −196 °C using a BELSORP-max sorptometer. Prior to analysis the samples were outgassed in vacuo for 4 h at 300 °C until a stable vacuum of 0.1 Pa was reached. Geometrical (pressure independent) and BJH method was used for the determination of pore diameter [34,35]. Temperature programmed reduction and metal dispersion experiment were also carried out using a BELSORP-max instrument. Prior to analysis, the samples were outgassed as that applied for Nitrogen physisorption measurement. Scanning electron micrographs were recorded using a Zeiss DSM 962 (Zeiss, Oberkochen, Germany). The sample was deposited on a sample holder with an adhesive carbon foil and sputtered with gold. Transmission electron microscopy was performed on a LEO Zeiss 912 AB. The samples were dispersed in ethanol and sonicated for 15 min and deposited on a copper grid before TEM imaging. The total sulfur concentration was determined with an ELEMENTAR Vario trace analyzer according to the ASTM D 5453.

3. Results and discussion

3.1. In situ synthesis

In situ incorporation of nickel nanoparticles into the mesopores of MCM-41 was carried out by alternating of hydrophilic property of synthesis medium which results in alternating solvent–solute interaction. Herein, solvent attributed to surfactant solution and solute referred to nickel precursor. $Ni(acac)_2$ was dissolved in toluene and used as precursor (solute) because of its very low solubility in water. $Ni(acac)_2$ dissolves inside the hydrophobic core CTAB micelles. However, there is a considerable amount of ethanol in synthesis medium, which can dissolve $Ni(acac)_2$ outside the micelles. About 90 vol.% of ethanol was distilled under vacuum which reduced the hydrophobic property of solvent and so caused diffusion of $Ni(acac)_2$ from solution into the CTAB micelles. Briefly, forming process of nickel nanoparticles in MCM-41 mesopores as follows: by addition of TEOS, $Ni(acac)_2$ was incorporated inside the mesopores of (as-synthesized) MCM-41. Then, the organic part of this complex as well as CTAB micelles, was burned out during calcination under air. It is supposed that the $Ni(acac)_2$ converts to NiO nanoparticles inside the mesopores of MCM-41. The graphical explanation is illustrated in Scheme 1.

In other words, decrease in the amount of ethanol decreases the solubility of $Ni(acac)_2$ outside the micelles. Additionally, due to the room temperature synthesis and relatively low synthesis time, no

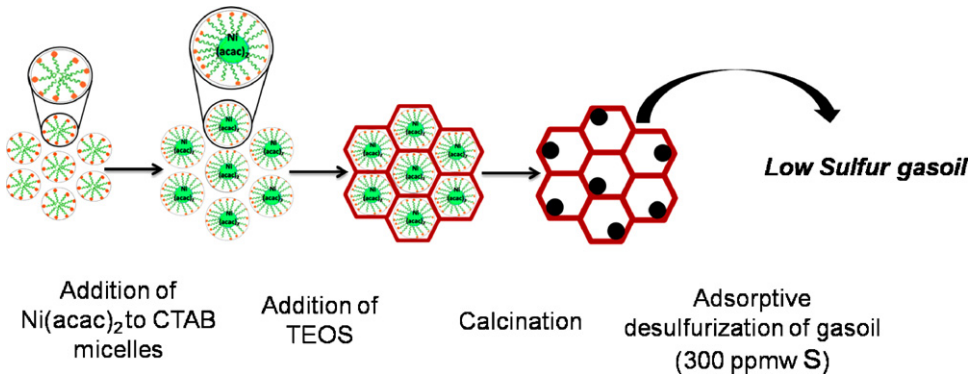

Scheme 1. Representation of in situ incorporation of nickel nanoparticles inside the mesopores of MCM-41.

considerable leaching of the $Ni(acac)_2$ was observed. The amount of nickel in the final product was measured by elemental analysis. Depending on the $Ni(acac)_2$ concentration in the initial synthesis solution, the 93–98 wt.% of added nickel (at the beginning of synthesis) was incorporated into MCM-41. The elemental analysis for determination of nickel was performed by atomic absorption spectrometry indicated that the samples Ni3/MCM, Ni6/MCM and Ni7/MCM contain 2.94, 5.7 and 6.51 wt.%, respectively. As the concentration of precursor in the synthesis solution increased, its incorporation into MCM-41 partially decreased.

3.2. XRD analysis

Low angle XRD patterns of calcined samples are shown in Fig. 1. High angle XRD patterns of the corresponding samples are also illustrated in Fig. 2. It is well-known that the number of peaks and their intensity represent the long-range structural order of MCM-41 [1–3]. Low angle diffractograms of parent MCM-41, Ni3/MCM and Ni6/MCM (Fig. 1a–c, respectively) exhibit intense d_{100} reflections with four small peaks located at the higher 2θ values. The low angle X-ray diffractograms display that the intensity of d_{100} reflections do not considerably decreased up to 6 wt.% of nickel loading. This means that Ni3/MCM and Ni6/MCM preserved their well-ordered hexagonal pore structure even after incorporation of nickel nanoparticles within their mesopores. In case of Ni7/MCM (Fig. 1d) the intensity of d_{100} reflection importantly decreased and the higher reflections almost disappeared. This might be due to the fact that CTAB micelles have a limited capacity for dissolving $Ni(acac)_2$. As the amount of loaded nickel increased the position of d_{100} reflections, which was applied for the determination of unit cell parameter, shift to lower 2θ angles. This observation might be due to the addition of $Ni(acac)_2$, which can act as swelling agent and increase the size of CTAB micelles. This phenomenon results in a MCM-41 with a larger pore diameter. The small peaks at high angle XRD patterns of Ni3/MCM, Ni6/MCM and Ni7/MCM (Fig. 2b–d), which can be indexed as (1 1 1), (2 0 0) and (2 2 0), relate to the presence of nickel oxide in MCM-41. As expected the intensity

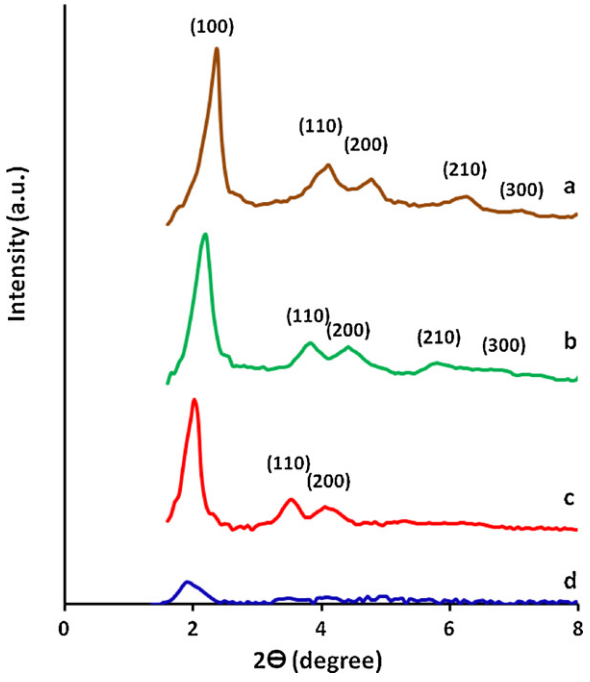

Fig. 1. Low angle PXRD patterns of (a) parent MCM-41, (b) Ni3/MCM, (c) Ni6/MCM, and (d) Ni7/MCM.

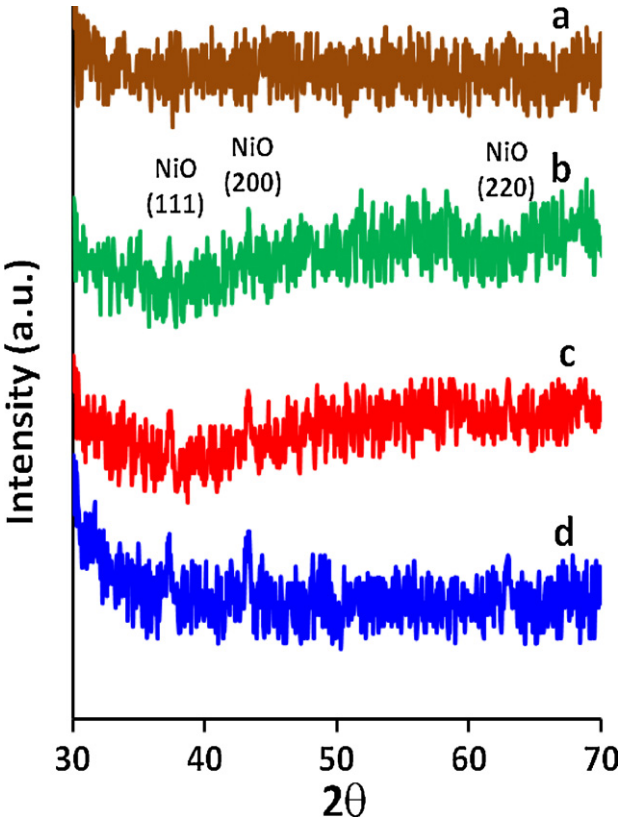

Fig. 2. High angle PXRD patterns of (a) parent MCM-41, (b) Ni3/MCM, (c) Ni6/MCM, and (d) Ni7/MCM.

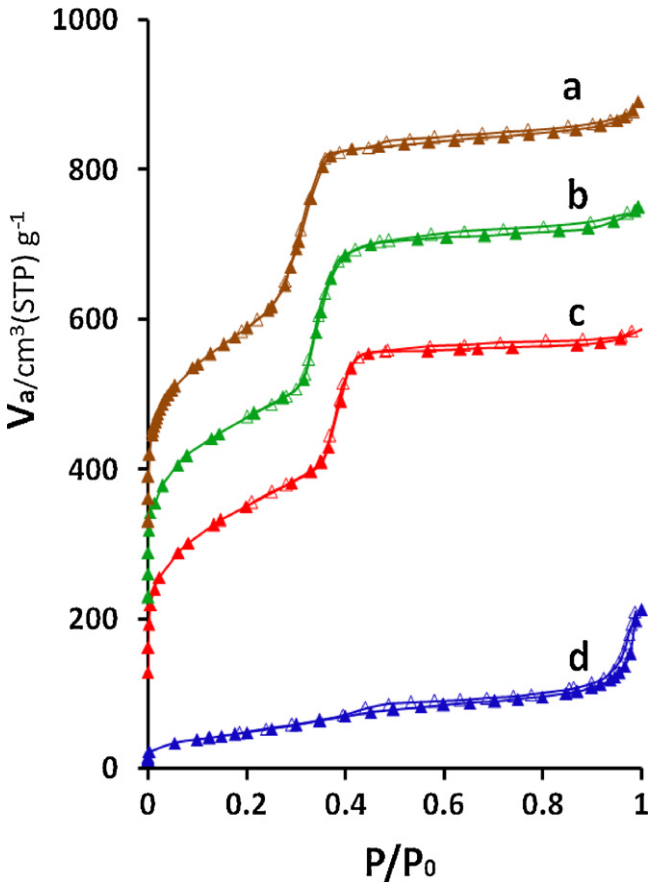

Fig. 3. Nitrogen physisorption isotherms of (a) parent MCM-41, (b) Ni3/MCM, (c) Ni6/MCM, and (d) Ni7/MCM. The isotherms for (b)–(d) are vertically offset by 100, 200 and 300 cm^3 (STP) g^{-1}, respectively.

of diffraction peaks due to nickel oxide amplified slightly as the amount of nickel increased.

3.3. N_2 physisorption

Fig. 3 demonstrates the nitrogen physisorption isotherms of parent MCM-41, Ni3/MCM, Ni6/MCM and Ni7/MCM. Parent MCM-41, Ni3/MCM and Ni6/MCM (Fig. 3a–c) exhibit the type IV isotherm, which is the typical characteristic of mesoporous materials. However, while Ni7/MCM represents an isotherm which is more or less similar to type IV, its shape is extremely distorted. Nitrogen adsorption at low pressures is usually assigned to monolayer–multilayer adsorption of nitrogen on the surface of sample (both on the external surface and inside the mesopores) which is proportional to surface area of corresponding sample. The specific surface area was calculated from the linear part of the BET (Brunauer–Emmett–Teller) equation (P/P_0 = 0.05–0.23) given in Table 1. The BET surface area of Ni3/MCM and Ni6/MCM are comparable to that of parent MCM-41. At higher relative pressure a sudden steep increase of the amount of adsorbed nitrogen is observed which is due to the capillary condensation of nitrogen inside the mesopores.

In case of parent MCM-41, Ni3/MCM and Ni6/MCM, filling of the mesopores takes place over a fairly narrow range of relative pressure. This happening indicates that the mesopores have both high structural order and uniform size. Pore size distributions (BJH) of all samples are illustrated in Fig. 4. As can be seen in Fig. 4a–c, parent MCM-41, Ni3/MCM and Ni6/MCM have narrow pore size distributions. Another indication for this statement is the fact that the desorption branch of the isotherm around capillary condensation

Table 1
Textural properties of all samples synthesized with the following Ni/MCM weight ratios: 0, 0.03, 0.06 and 0.07.

Sample	S_{BET} (m^2/g)[a]	V_t (cm^3/g)[b]	a (nm)[c]	W_d (nm)[d]
MCM-41	1103	0.93	4.28	3.61
Ni3/MCM	1080	0.91	4.63	3.81
Ni6/MCM	1064	0.84	4.92	3.98
Ni7/MCM	215	0.33	5.10	2.50

[a] BET specific surface area.
[b] Total pore volume.
[c] Unit cell parameter obtained from XRD diffractograms ($2d_{100}/\sqrt{3}$).
[d] Pore diameter (nm) calculated by geometrical (pressure independent) method.

step nearly coincides with the adsorption branch, which reveals the reversible nitrogen adsorption inside the mesopores. Furthermore, this reversible behavior suggests that most pores within the samples are open pores, connected directly to the surface of the MCM-41 and so are accessible for the guest molecules such as nitrogen. This means that no significant pore blocking was occurred by incorporated nickel nanoparticles in mesopores of MCM-41 even at high nickel loadings (Ni6/MCM).

The presence of toluene, which acts as swelling agent causes no significant structural disordering, which implies that an appropriate approach was applied for incorporation of nickel nanoparticles into MCM-41. However, the height of the capillary condensation/evaporation step slightly decreased as the amount of loaded nickel increased. In other words, the mesopore volume decreased slightly as the amount of nickel increased (Table 1).

Fig. 3d, related to the Ni7/MCM, shows that the shape of the isotherm (in capillary condensation/evaporation step) broadened. This phenomenon is caused by high loading of nickel which results in severe shrinkage of hexagonal structure. Fig. 4d also indicates the broad pore size distribution of this sample. These results are in agreement with those found from the low angle XRD patterns (Fig. 1d). The textural properties of all samples are given in Table 1.

3.4. H_2-TPR measurement

Fig. 5 illustrates the results of *H2-1 TPR* test on the Ni3/MCM, Ni6/MCM and Ni7/MCM. As can be seen, each Ni3/MCM (Fig. 5a)

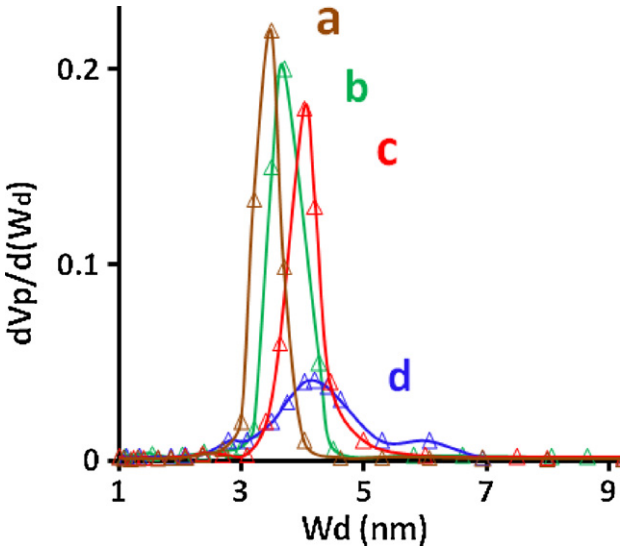

Fig. 4. Pore size distributions of (a) (brown curve) parent MCM-41, (b) (green) Ni3/MCM, (c) (red curve) Ni6/MCM, (d) (blue curve) Ni7/MCM that obtained from BJH (desorption branch) method. (For interpretation of the references to color in this figure legend, the reader is referred to the web version of the article.)

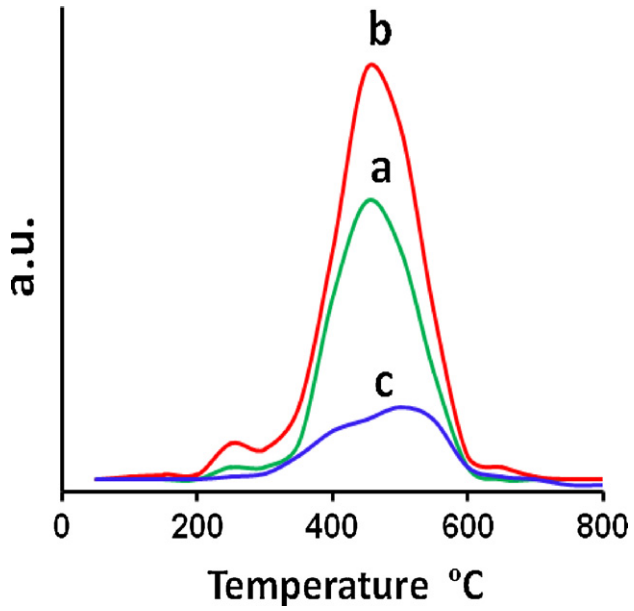

Fig. 5. Temperature programmed reduction curves of (a) Ni3/MCM, (b) Ni6/MCM and (c) Ni7/MCM.

and Ni6/MCM (Fig. 5b) shows two major reduction peaks that begin from ca. 200 °C and 327 °C, respectively.

As expected, Ni6/MCM absorbed a higher amount of hydrogen than Ni3/MCM. In the case of Ni7/MCM, this behavior was reversed. In other words, Ni7/MCM (Fig. 5c) shows a weaker reduction peak than Ni3/MCM and Ni6/MCM. An explanation might be that this reduction is due to the distortion of the hexagonal mesopores of Ni7/MCM. A suggestion might be that the distortion hexagonal mesopores leads to the formation of dead pores rather than open pores and consequently nickel nanoparticles, which incorporated into these dead pores, become inaccessible for hydrogen molecules.

In the case of 3 and 6 wt.% loading of nickel, loss of the pore ordering was not considerably occurred as compared to pure MCM-41 and three reflections (in XRD diffractograms) of the hexagonal structure are discerned. Increasing the $Ni(acac)_2$/toluene loading to 7 wt.% also causes a significant broadening and weakness of the (1 0 0) reflection as expected for the addition of swelling agents. This might be due to the fact that CTAB micelles have limited capacity for dissolving the $Ni(acac)_2$ and toluene. As a result, cylindrical shape of CTAB micelles was distorted and the final MCM-41 product had very disordered structure.

From hydrogen chemisorptions experiments, metal dispersion (fraction of active surface metal atoms) of 33%, 29% and 6% were measured for Ni3/MCM, Ni6/MCM and Ni7/MCM, respectively. This means that considerable quantities of nickel nanoparticles are accessible for hydrogen molecules in Ni3/MCM, Ni6/MCM while, many of them are out of reach of hydrogen molecules in the case of Ni7/MCM.

3.5. TEM imaging

Transmission electron microscopy was performed on parent MCM-41, Ni3/MCM, Ni6/MCM and Ni7/MCM for direct elucidation of the hexagonal array of mesopores as well as position of nickel nanoparticles. TEM images of all samples are shown in Fig. 6. Fig. 6a provides side view of mesopores of parent MCM-41. It can be seen that the nickel nanoparticles (dark points) were embedded within the mesopores (Fig. 6b). However, as the amount of nickel increased (Fig. 6c) the nanoparticles merged together and formed larger nanoparticles.

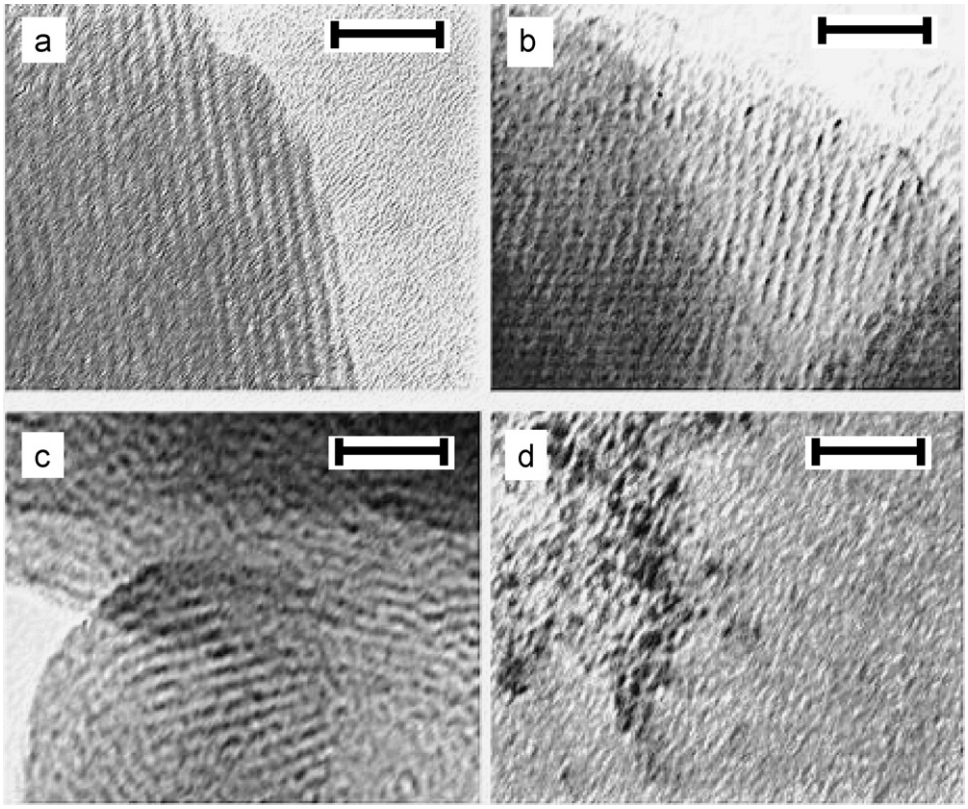

Fig. 6. TEM images of (a) parent MCM-41, (b) Ni3/MCM, (c) Ni6/MCM, and (d) Ni7/MCM. The scale bar represents 32 nanometers. Dark points related to the nickel oxide nanoparticles.

Fig. 6d shows that the hexagonal structure got extremely damaged, as the amount of nickel reached to 7 wt.% (Ni7/MCM). Additionally, the size of nickel nanoparticles increased and their dispersion decreases. This occurrence might be due to the lack of hindrance effect of broken hexagonal mesopores. This observation further supports the weaker reduction peak of nickel nanoparticles (Fig. 5c) in chemisorption experiment.

3.6. Desulfurization

As mentioned in Section 2, the effect of three parameters, i.e., nickel concentration, temperature and feed flow rate on desulfurization process was examined. For the investigation of the effect of nickel concentration on the desulfurization process, the breakthrough sulfur adsorption capacity and the total sulfur adsorption capacity (integrated area between the breakthrough curve and the dashed line, representing the initial sulfur concentration of the feed) of three synthesized MCM-41 samples, which contained different amounts of nickel were determined at 150 °C and 0.3 ml/min flow rate of feed. The results are shown by the bar chart in Fig. 7. Ni7/MCM has the lowest breakthrough and total sulfur adsorption capacity, which is due to the inaccessibility of nickel nanoparticles for MDBT molecules. This might be caused by damage of ordered mesopores of MCM-41 which results in confinement of a large number of nickel nanoparticles in the dead pores. Their size was also increased which was expected to be a drawback for MDBT adsorption.

As can be seen, the breakthrough sulfur adsorption capacity of Ni6/MCM is higher than twice that of Ni3/MCM ($0.56 > 0.26 \times 2$). In the case of total sulfur adsorption capacity, this relation is inversed. In other words, total sulfur adsorption capacity of Ni6/MCM is twice smaller than that of Ni3/MCM ($1.55 < 0.81 \times 2$). This small difference between the breakthrough sulfur adsorption capacity and the total sulfur adsorption capacity might be attributed to the large size of the MDBT molecule. We suggest that although the pore size of MCM-41 is large, at the beginning of adsorption, a lot of MDBT molecules are rapidly adsorbed on the nickel nanoparticles near the pore entrance so the breakthrough sulfur adsorption capacity of Ni6/MCM becomes greater than that of Ni3/MCM. After that, when the adsorption of MDBT proceeds, a small number of those nickel nanoparticles, which are located deep inside far from the entrance, are not accessible to the MDBT molecules. However as mentioned above, the pore blockage is not considerable, because the difference between the breakthrough sulfur adsorption capacity and the total sulfur adsorption capacity is small. Based on these results, Ni6/MCM was selected as the best adsorbent for the following adsorption experiments in order to investigate its adsorption capacity at various temperatures and flow rates. As the boiling range of feed was 220–370 °C, the maximum adsorption temperature was limited to 200 °C to minimize the loss of feed by vaporization.

Figs. 8 and 9 illustrate the sulfur adsorption capacity of Ni6/MCM at 1 and 0.3 ml/min feed flow rates, respectively. As the flow rate of the feed decreased, the sulfur adsorption capacity increased. This might be explained by the higher contact time between the feed and the adsorbent.

The effect of temperature was also investigated in both flow rates. As can be seen in Figs. 8 and 9, at 25 °C, the sulfur breakthrough occurred instantly after the feed solution was eluted, and the sulfur concentration in the effluent increased rapidly. This occurrence was observed in both flow rates which might be deduced that no significant adsorption was occurred at room temperature. As the temperature of absorption increased, the sulfur breakthrough was occurred later. This behavior was also observed at both flow rates.

The latest sulfur breakthrough volume, obtained at 200 °C and 0.3 ml/min flow rate of feed, was about 5.4 ml/g (Fig. 9, red curve). The enhanced adsorption of MDBT at higher temperatures strongly suggests that the major interaction involved between the nickel incorporated MCM-41 and the MDBT should be chemisorption or reactive adsorption [36]. In addition, a lower flow rate (0.3 ml/min) results in a later sulfur breakthrough. This phenomenon was expected due to the fact that as the flow rate decreased, the contact

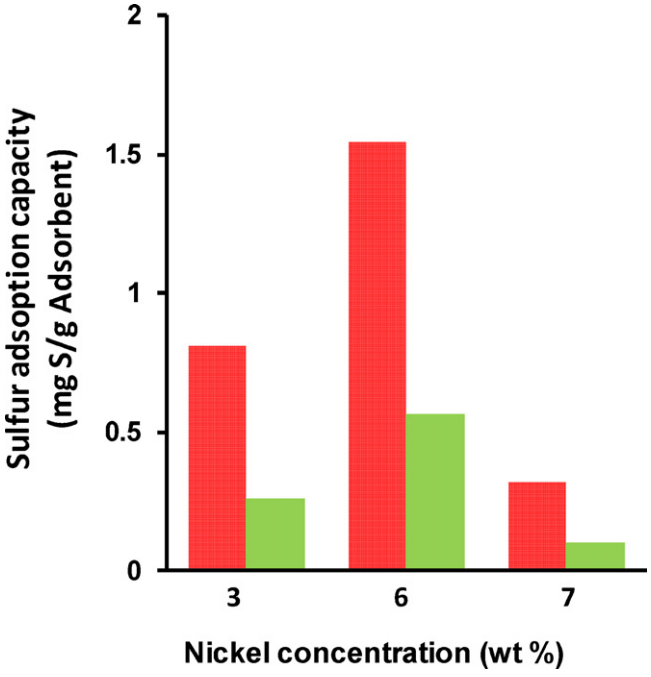

Fig. 7. Breakthrough sulfur adsorption capacities (green bars) and total sulfur adsorption capacities (red bars) of Niy/MCM with three different nickel concentrations at 150 °C (gas oil containing 300 ppmw sulfur was used as feed solution). (For interpretation of the references to color in this figure legend, the reader is referred to the web version of the article.)

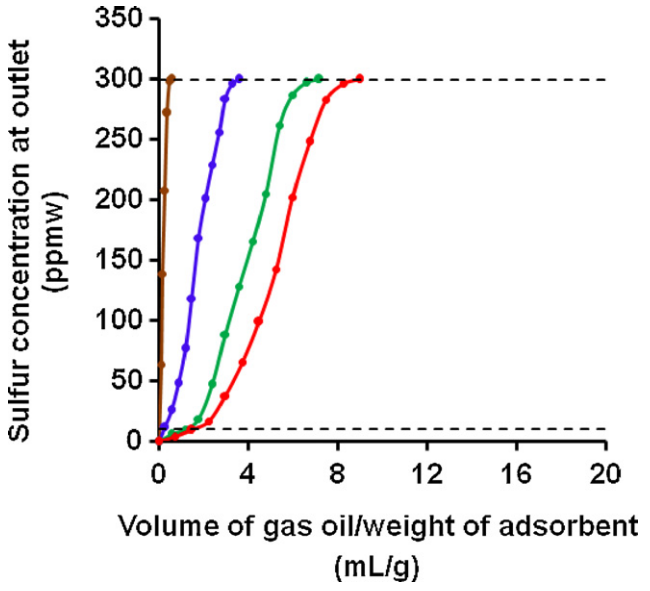

Fig. 8. Breakthrough curves for the adsorptive desulfurization of gas oil containing 300 ppmw sulfur over Ni6/MCM at 1 ml/min flow rate of feed and four different temperatures as follow: 25 °C (brown curve), 75 °C (blue curve), 150 °C (green curve) and 200 °C (red curve). Dashed line at the top of the chart indicates the initial sulfur concentration of feed and the dotted line at the bottom of the chart indicates the sulfur breakthrough (10 ppmw). (For interpretation of the references to color in this figure legend, the reader is referred to the web version of the article.)

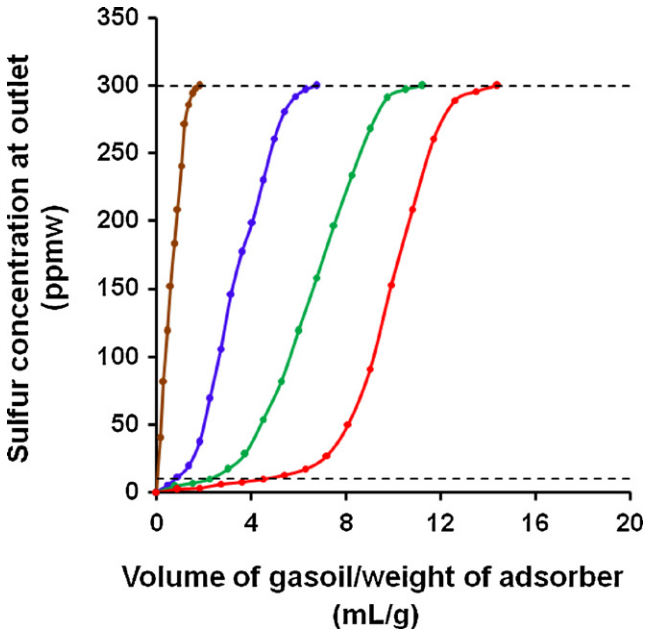

Fig. 9. Breakthrough curves of Ni6/MCM at 0.3 ml/min flow rate of feed and four different temperatures as follow: 25 °C (brown curve), 75 °C (blue curve), 150 °C (green curve) and 200 °C (red curve) (gas oil containing 300 ppmw sulfur was used as feed solution). Dashed line at the top of the chart indicates the initial sulfur concentration of feed and the dotted line at the bottom of the chart indicates the sulfur breakthrough (10 ppmw). (For interpretation of the references to color in this figure legend, the reader is referred to the web version of the article.)

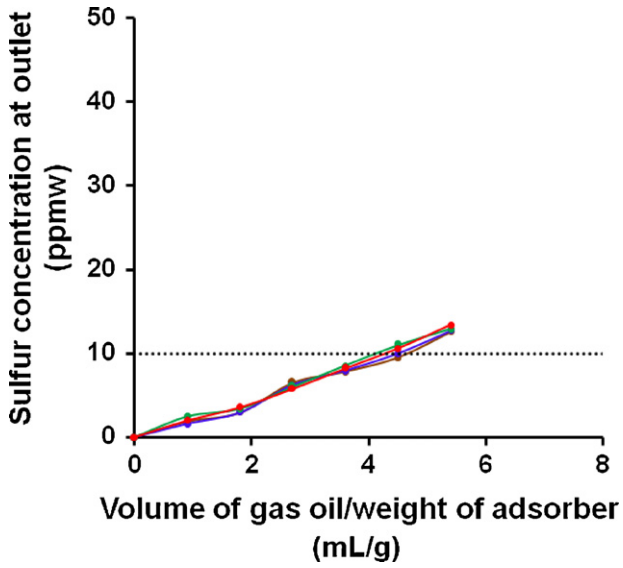

Fig. 10. Breakthrough curves for the adsorptive desulfurization of gas oil containing 300 ppmw of sulfur at 200 °C over a regenerated Ni6/MCM adsorbent (treated at 500 °C in flowing hydrogen gas for 2 h) at four cycles (red, blue, green and red curves corresponded to first, second, third and forth cycles, respectively). Dotted line at the bottom of the chart represents the sulfur breaktrough (10 ppmw). (For interpretation of the references to color in this figure legend, the reader is referred to the web version of the article.)

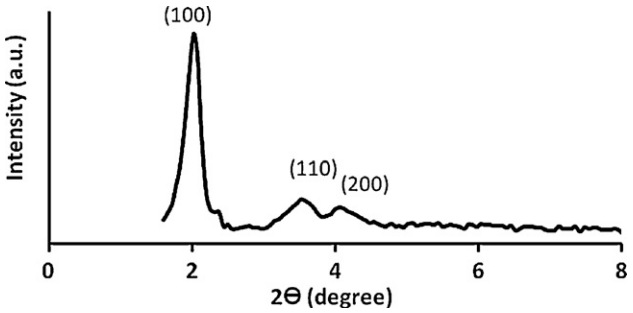

Fig. 11. PXRD pattern of Ni6/MCM after four times of regeneration and desulfurization.

time between the feed and adsorbent increased. This increasing in the contact time results in higher sulfur removal capacity. Additionally, the value of the sulfur breakthrough was considerable, contrasting with the quantity of nickel loaded into mesoporous silica (6 wt.%). This occurrence might be an indication of a high dispersion of nickel nanoparticles inside the mesopores of MCM-41 and proper accessibility of them for MDBT molecules without significant pore blocking during adsorption so, this seems to be the main reason for substantial breakthrough sulfur adsorption capacity. Furthermore, direct interaction of sulfur atom with nickel nanoparticles is the main interaction in adsorptive desulfurization. The smaller size of nanoparticles can improves the selectivity of adsorbent for removal of a refractory sulfur compound with high steric hindrance and high molecular weight, i.e., MDBT. Thus, a proper synthesis approach which results in incorporation of well-dispersed as well as small nickel nanoparticles into the MCM-41, can strongly enhance the capacity of adsorbent toward adsorptive desulfurization. The total sulfur adsorption capacity and breakthrough sulfur adsorption capacity which obtained in this work is higher than those analogous methods which carried out with nickel-doped mesoporous silica (obtained via wet impregnation of mesoporous silica) with similar metal loadings [34,35]. We can suggest that one of the main reasons for higher sulfur adsorption capacity might be the suitable method which applied for incorporation of nickel nanoparticles into MCM-41.

Upon the results obtained from the H_2-TPR experiments, the reductive regeneration of the spent adsorbent was performed by flowing hydrogen at 500 °C for 2 h.

Fig. 10 displays the breakthrough curves of the regenerated adsorbent in four cycles, indicating that the adsorption performance can be recovered by the regeneration. To understand the loss of nickel content of Ni6/MCM after four times regeneration, the sample was analyzed using atomic absorption spectrometry. No nickel was detectable by this method. However, the lack of decreasing of breakthrough sulfur adsorption capacity indicates that nickel leaching was not taken place even after four times regeneration. Figure also indicates the XRD pattern of Ni6/MCM after four times regeneration and desulfurization. Presence of four diffraction peaks implies that the well-ordered hexagonal structure of Ni6/MCM was almost preserved (Fig. 11).

4. Conclusion

In the present work, nickel nanoparticles were incorporated inside the mesopores of MCM-41 via a modified in situ approach. The selection of a hydrophobic complex, i.e., $Ni(acac)_2$ as nickel precursor was a key factor toward incorporation of nickel nanoparticles inside the mesopores of MCM-41 by manipulation of solvent–solute interaction in synthesis medium. Three nickel-containing samples were characterized with powder XRD, nitrogen physisorption, temperature programmed reduction, TEM and atomic absorption spectrometry. The results showed that the samples had 3 wt.% and 6 wt.% of nickel and preserved their well-ordered hexagonal structure. Additionally, their BET surface area was comparable with the parent MCM-41. Nickel nanoparticles were formed and evenly distributed into the mesopores of MCM-41 and did not cause considerable pore blocking. It is proved that synthesized samples might be used for adsorptive desulfurization of

gas oil contains 300 ppmw of refractory sulfur compound (MDBT). Three Ni*y*/MCM samples exhibited different adsorption capacities for sulfur removal, which depends not only on the concentration of nickel but also on their textural properties. The highest breakthrough sulfur adsorption capacity obtained at 200 °C and 0.3 ml/min flow rate of feed, was 0.69 mg/g for the Ni6/MCM. The regenerated Ni6/MCM (reduced at 500 °C with hydrogen) showed almost the same breakthrough sulfur adsorption capacity even after four cycles of regeneration. The substantial adsorption capacity of the synthesized samples in spite of their low nickel quantity might be related to the proper approach applied for the synthesis of samples which results in the formation of small and well-dispersed nickel nanoparticles inside the mesopores of MCM-41. As the smaller size of nanoparticles, the higher adsorption capacity toward refractory sulfur compounds like MDBT. This is due to both the increase in the number of active sites for adsorption and also the decrease of space hindrance during the interaction of nickel nanoparticles with sulfur atoms that are surrounded by benzene and methyl groups in MDBT molecules. Substantial adsorption capacity of synthesized samples for sulfur removal imply that appropriate route was applied for the incorporation of nickel into mesoporous silica which results in well-dispersed and, accessible and small nanoparticles incorporated into MCM-41. It is well known that easy and complete regeneration of the adsorbent is of vital importance for adsorptive desulfurization. The spent adsorbent was also recovered its adsorption capacity even after four cycles of reductive regeneration.

References

[1] C.T. Kresge, M.E. Leonowicz, W.J. Roth, J.C. Vartuli, J.S. Beck, Ordered mesoporous molecular sieves synthesized by a liquid-crystal template mechanism , Nature 359 (1992) 710–712.

[2] T. Yanagisawa, T. Shimizu, K. Kuroda, C. Kato, The preparation of alkyltriinethylaininonium–kaneinite complexes and their conversion to microporous materials , Bull. Chem. Soc. Jpn. 63 (1990) 988–992.

[3] J.S. Beck, J.C. Vartuli, W.J. Roth, M.E. Leonowicz, C.T. Kresge, K.D. Schmitt, C.T.W. Chu, D.H. Olson, E.W. Sheppard, S.B. McCullen, J.B. Higgins, J.L. Schlenker, A new family of mesoporous molecular sieves prepared with liquid crystal templates , J. Am. Chem. Soc. 114 (1992) 10834–10843.

[4] A. Corma, From microporous to mesoporous molecular sieve materials and their use in catalysis , Chem. Rev. 97 (1997) 2373–2420.

[5] Y. Wan, D.Y. Zhao, On the controllable soft-templating approach to mesoporous silicates , Chem. Rev. 107 (2007) 2821–2860.

[6] A. Taguchi, F. Schuth, Ordered mesoporous materials in catalysis , Microporous Mesoporous Mater. 77 (2005) 1–45.

[7] K. Nakanishi, N. Tanaka, Sol–Gel with phase separation. hierarchically porous materials optimized for high-performance liquid chromatography separations , Acc. Chem. Res. 40 (2007) 863–873.

[8] M.A. Zanjanchi, A. Ebrahimian, Z. Alimohammadi, A spectroscopic study on the adsorption of cationic dyes into mesoporous AlMCM-41 materials , Opt. Mater. 29 (2007) 794–800.

[9] J. Lu, M. Liong, J.I. Zink, F. Tamanoi, Mesoporous silica nanoparticles as a delivery system for hydrophobic anticancer drugs , Small 8 (2007) 1341–1346.

[10] D. Crespo, G.Q. Yuhe, W. Frances, H. Yang, R.T. Yang, Superior sorbent for natural gas desulfurization , Ind. Eng. Chem. Res. 47 (2008) 1238–1244.

[11] T.R. Ling, B.Z. Wan, H.P. Lin, C.Y. Mou, Desulfurization of vacuum gasoil by MCM-41 supported molybdenum–nickel catalysts , Ind. Eng. Chem. Res. 48 (2009) 1797–1803.

[12] F. Somma, G. Strukul, Oxidation of geraniol and other substituted olefins with hydrogen peroxide using mesoporous, sol–gel-made tungsten oxide–silica mixed oxide catalysts , J. Catal. 227 (2004) 344–351.

[13] M. Mamak, G.S. Metraux, S. Petrov, N. Coombs, G.A. Ozin, M.A. Green, Lanthanum strontium manganite/yttria-stabilized zirconia nanocomposites derived from a surfactant assisted, co-assembled mesoporous phase , J. Am. Chem. Soc. 125 (2003) 5161–5175.

[14] L. Bronstein, E.K. Emer, B. Berton, C. Burger, S.F. Erster, M. Antonietti, Successive use of amphiphilic block copolymers as nanoreactors and templates: preparation of porous silica with metal nanoparticles , Chem. Mater. 11 (1999) 1402–1405.

[15] P. Krawiec, E. Kockrick, P. Simon, G. Auffermann, S. Kaskel, Platinum-catalyzed template removal for the in situ synthesis of MCM-41 supported catalysts , Chem. Mater. 18 (2006) 2663–2669.

[16] I. Yuranov, P. Moeckli, S.E. Buffat, P. Kiwi-Minsker, L. Renken, Pd/SiO_2 catalysts: synthesis of Pd nanoparticles with the controlled size in mesoporous silicas , J. Mol. Catal. A: Chem. 192 (2003) 239–251.

[17] H. Chen, A. Matsumoto, N. Nishimiya, K. Tsutsumi, A novel ion exchange method to modify mesoporous molecular sieve Al-FSM-16 by cobalt-complex , Chem. Lett. 9 (1999) 993–994.

[18] W.H. Zhang, J.L. SHI, L.Z. Wang, D.S. Yan, Preparation and characterization of ZnO clusters inside mesoporous silica , Chem. Mater. 12 (2000) 1408–1413.

[19] L. Zhang, T. Sun, J.Y. ying, Oxidation catalysis over functionalized metalloporphyrins fixated within ultralarge-pore transition metal-doped silicate supports , Chem. Commun. (1999) 1103–1104.

[20] Y. Zhang, F.L.-Y. Lam, X. Hu, Z. Yan, P.J. Sheng, Fabrication of copper nanowire encapsulated in the pore channels of SBA-15 by metal organic chemical vapor deposition , J. Phys. Chem. C 111 (2007) 12536–12541.

[21] M.E. Grass, Y. Yue, S.E. Habas, R.M. Rioux, C.I. Teall, P. Yang, G.A. Somorjai, Silver ion mediated shape control of platinum nanoparticles: removal of silver by selective etching leads to increased catalytic activity , J. Phys. Chem. C 112 (2008) 4797–4804.

[22] L. Li, J.-L. Shi, L.-X. Zhang, L.-M. Xiong, J.-N. Yan, A novel and simple in-situ reduction route for the synthesis of an ultra-thin metal nanocoating in the channels of mesoporous silica materials , Adv. Mater. 16 (2004) 1079–1082.

[23] G.E. Fryxell, The synthesis of functional mesoporous materials , Inorg. Chem. Commun. 9 (2006) 1141–1150.

[24] Z.-j. Wang, Y. Xie, C.-j. Liu, Synthesis and characterization of noble metal (Pd, Pt, Au, Ag) nanostructured materials confined in the channels of mesoporous SBA-15 , J. Phys. Chem. C 112 (2008) 19818–19824.

[25] M.S. Holm, E. Taarninga, K. Egeblada, C.H. Christensena, Catalysis with hierarchical zeolites , Catal. Today 168 (2011) 3–16.

[26] A. Infantes-Molina, J.A. Cecilia, B. Pawelec, J.L.G. Fierro, E. Rodríguez-Castellón, A. Jiménez-López, Ni_2P and CoP catalysts prepared from phosphite-type precursors for HDS–HDN competitive reactions , Appl. Catal. A: Gen. 390 (2010) 253–263.

[27] Z. Vít, D. Gulková, L. Kaluža, S. Bakardieva, M. Boaro, Mesoporous silica–alumina modified by acid leaching as support of Pt catalysts in HDS of model compounds , Appl. Catal. B: Environ. 100 (2010) 463–471.

[28] C. Song, An overview of new approaches to deep desulfurization for ultra-clean gasoline, diesel fuel and jet fuel , Catal. Today 86 (2003) 211–263.

[29] R.L. Irvin, Process for desulfuring gasoline and hydrocarbon feedstocks, U.S. Patent 5,730,860 (1998).

[30] S. Velu, S. Watanabe, X. Ma, C. Song, Regenerable adsorbents for the deep desulfurization of transportation fuels for fuel cell applications , Prepr. Pap. Am. Chem. Soc.: Div. Fuel Chem. 48 (2003) 526–528.

[31] J.G. Park, C.H. Ko, K.B. Yi, J.-H. Park, S.-S. Han, S.-H. Cho, J.-N. Kim, Reactive adsorption of sulfur compounds in diesel on nickel supported on mesoporous silica , Appl. Catal. B: Environ. 81 (2008) 244–250.

[32] C. Sentorun-Shalaby, S.K. Saha, X. Ma, C. Song, Mesoporous-molecular-sieve-supported nickel sorbents for adsorptive desulfurization of commercial ultra-low-sulfur diesel fuel , Appl. Catal. B: Environ. 101 (2011) 718–726.

[33] V.M. Bhandari, C.H. Ko, J.G. Park, S.-S. Han, S.-H. Cho, J.-N. Kim, Desulfurization of diesel using ion-exchanged zeolites , Chem. Eng. Sci. 61 (2006) 2599–2608.

[34] A. Galarneau, D. Desplantier, R. Dutartre, F. Direnzo, Micelle templated silicates as a test bed for methods of mesopore size evaluation , Microporous Mesoporous Mater. 27 (1999) 297–308.

[35] G.C. Sonwane, S.K. Bhatia, Characterization of pore size distributions of mesoporous materials from adsorption isotherms , J. Phys. Chem. B 104 (2000) 9099–9110.

[36] S. Velu, X. Ma, C. Song, M. Namazian, S. Sethuraman, G. Venkataraman, Desulfurization of JP-8 Jet fuel by selective adsorption over a Ni-based adsorbent for micro solid oxide fuel cells , Energy Fuels 19 (2005) 1116.